Three-dimensional velocity structure of the outer fore arc of the Colombia-Ecuador subduction zone and implications for the 1958 megathrust earthquake rupture zone

Lina Constanza García Cano, Audrey Galvé, Philippe Charvis, Boris Marcaillou

AGU PUBLICATIONS

JGR

Journal of Geophysical Research: Solid Earth

RESEARCH ARTICLE
10.1002/2012JB009978

Key Points:
- Impact of upper plate structure on great earthquakes rupture zone

Supporting Information:
- Readme
- Figure S1
- Figure S2

Correspondence to:
A. Galve,
audrey.galve@geoazur.unice.fr

Citation:
García Cano, L. C., A. Galve, P. Charvis, and B. Marcaillou (2014), Three-dimensional velocity structure of the outer fore arc of the Colombia-Ecuador subduction zone and implications for the 1958 megathrust earthquake rupture zone, *J. Geophys. Res. Solid Earth*, *119*, 1041–1060, doi:10.1002/2012JB009978.

Received 14 DEC 2012
Accepted 28 NOV 2013
Accepted article online 6 DEC 2013
Published online 7 FEB 2014

Three-dimensional velocity structure of the outer fore arc of the Colombia-Ecuador subduction zone and implications for the 1958 megathrust earthquake rupture zone

Lina Constanza García Cano[1,2], Audrey Galve[1], Philippe Charvis[1], and Boris Marcaillou[3,4]

[1]Université Nice Sophia Antipolis, IRD, CNRS, Observatoire de la Côte d'Azur, Valbonne, France, [2]Now at Observatorio Vulcanológico y Sismológico de Manizales-Servicio Geológico Colombiano, Manizales, Colombia, [3]Campus de Fouillole, Université Antilles-Guyane, Pointe-à-Pitre, France, [4]Now at Université Nice Sophia Antipolis, IRD, CNRS, Observatoire de la Côte d'Azur, Géoazur, Nouméa, New Caledonia

Abstract In 2005, an onshore, offshore 3-D refraction and wide-angle reflection seismic experiment was conducted along the convergent margin at the border between Colombia and Ecuador, over the rupture zone of the 1958, M_w 7.6 subduction earthquake. A well-defined *Vp* velocity model of the plate boundary and upper and lower plates was constructed, down to 25 km depth, using first arrival traveltimes inversion. The model reveals a several kilometers thick, low-velocity zone in the upper plate, located immediately above the interplate contact. This low-velocity zone might be related to alteration and fracturing of the mafic and ultramafic rocks, which composed the upper plate in this area by fluids released by the lower plate with possible contributions from sediment underplating. Near the toe of the margin, the model shows a low-velocity gradient in the outer wedge, which is interpreted as highly faulted and fractured rocks. This low-velocity/low-gradient region appears to limit the oceanward extension of the rupture zones of the 1958 and 1979 earthquakes, possibly because coseismic deformation and uplift of the outer margin wedge dissipates most of the seismic energy.

1. Introduction

For more than two decades many authors have debated the potential influence of geologic structure on the initiation and propagation of earthquake ruptures, and especially of megathrust earthquakes occurring along the interplate seismogenic zone. Seismic asperities are areas of high seismic slip or high seismic moment release [*Lay and Kanamori*, 1981]. Some authors suggest that these asperities are related to geologic features such as strong crust in the upper plate [e.g., *Beck and Christensen*, 1991; *Byrne et al.*, 1988; *Ryan and Scholl*, 1993], subducted seamounts [*Cloos*, 1992; *Cloos and Shreve*, 1996], or large, smooth surfaces created by subducted sediments [*Ruff*, 1989]. There is also statistical evidence that most of the coseismic slip of several very large earthquakes ($M_w \geq 7.5$) occurred preferentially beneath fore-arc sedimentary basins which are interpreted to be areas of sustained subsidence of the continental slope and shelf resulting from basal erosion of the upper plate [*Wells et al.*, 2003].

Recently, the role of fluids in subduction zones has been interpreted to play a key role in the seismogenic zone behavior. A conceptual model based on the Nicaragua and Costa Rica margins [*Ranero et al.*, 2008] suggests that fluids released from the subducting plate migrate through the overriding plate. These pressurized fluids favor hydrofracturing and contribute to the basal erosion of the margin [*Ranero et al.*, 2008].

Subduction megathrust faults are located at depths ranging from 0 km at the trench to several tens of kilometers beneath the seafloor. To better understand the role of the convergent margin structure on the occurrence and magnitude of large earthquakes, we need active source seismic surveys with dense ocean bottom seismometer (OBS) network to obtain images of the geometry of the subduction fault and the velocity structure of the adjacent crusts [e.g., *Gailler et al.*, 2007; *Kopp et al.*, 2011; *Kamei et al.*, 2012]. Many active source seismic experiments have been conducted over convergent margins, but most of them are 2-D seismic experiments which do not map the extension and the variability of geologic features along strike. Only a small number of 3-D refraction experiments have been carried out along subduction zones, e.g., in

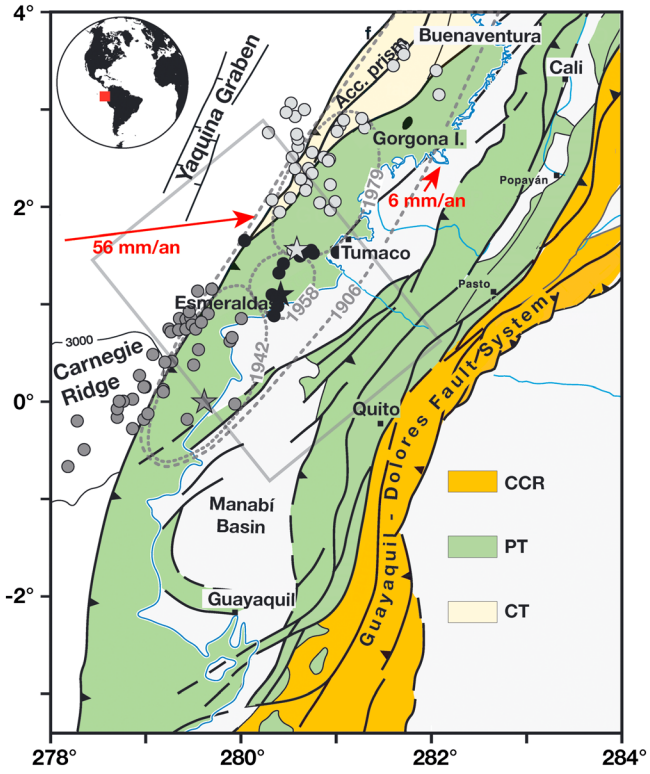

Figure 1. Geological sketch of North Ecuador and South Colombia showing the main accreted terranes, sedimentary basins, and faults after *Cediel et al.* [2003]. CCR: central continental realm; PT: Pacific Terranes which composed the North Andean Block (including Piñon and Gorgona formations); CT: Choco Terranes (including the small accretionnary prism which develops offshore Colombia). Red arrows represent velocity of the Nazca Plate and the North Andean Block relative to South America [*Nocquet et al.*, 2009]. The 3-D box used for the tomographic inversion is outlined in grey. Rupture zones of the 1906, 1942, 1958, and 1979 earthquakes are contoured by dashed grey lines. Main shocks (stars) and aftershocks (closed circles) of the 1942 (dark gray); 1958 (black) and 1979 (light gray) earthquakes are shown inferred from previous studies [*Beck and Ruff*, 1984; *Mendoza and Dewey*, 1984].

Chile near Valparaiso [*Zelt et al.*, 1999] or more recently along the Lesser Antilles fore arc [*Evain et al.*, 2013] or on the Sumatra fore arc [*Tang et al.*, 2013]. In this paper we present the results of a 3-D refraction survey along the Ecuador-Colombia convergent margin located over the rupture of the 1958 subduction earthquake and the boundary with the rupture of the 1979 earthquake, in order to produce a volumetric image of the seismic velocity structure of this part of the subduction zone.

2. Seismological and Tectonic Setting

2.1. Tectonic Setting

From Peru to Colombia, the subduction of the Nazca plate beneath the North Andean margin generates an active volcanic arc and intense seismic activity. Near the border between Colombia and Ecuador, the two plates converge along a N83°E direction at a rate of ~56 mm/yr (Figure 1) [*Nocquet et al.*, 2009; *Trenkamp et al.*, 2002].

The structure of the two plates contributes to the segmentation of the margin offshore Ecuador and southern Colombia [*Gailler et al.*, 2007]. In this area, the subducting segment of the Nazca plate is ~26 Myr old [*Lonsdale*, 2005] and shows a major E-W oriented topographic feature, the so-called Carnegie Ridge, which has formed by the interaction of the Galapagos hot spot with the Cocos-Nazca spreading center since ~20 Ma [e.g., *Sallarés and Charvis*, 2003]. The subduction of the Carnegie Ridge beneath the Ecuadorian coast, which started at least 2 Myr ago [*Sallarés and Charvis*, 2003; *Lonsdale*, 2005], induces lateral variations along the margin in seismicity, arc magmatism, deformation, vertical motion, and sediment distribution [*Collot et al.*, 2002; *Gutscher et al.*, 1999]. Because of the drift of the North Andean Block to the NW, the study area was affected by the subduction of the Carnegie Ridge in the past [*Michaud et al.*, 2009]. Seamounts also exist in the oceanic basin located north of the Carnegie Ridge, and one seamount buried at shallow depth in the subduction channel was imaged by seismic data in the study area [*Collot et al.*, 2008].

In this area, offshore Esmeraldas, the oceanic sedimentary cover is ~2 km thick and reaches 3 km thick in the trench where deep sea turbidites accumulate [*Collot et al.*, 2008]. Previous studies have shown that the Ecuador margin is erosional [*Collot et al.*, 2002, 2008; *Moberly et al.*, 1982] whereas north of 2°N, the Colombia margin is dominantly accretionary [*Marcaillou*, 2003; *Westbrook et al.*, 1995]. A 1.3 km thick, low-velocity (3.5–4.0 km/s) subduction channel is described beneath the margin outer wedge [*Collot et al.*, 2008; *Agudelo et al.*, 2009]. This subduction channel is likely related to subducted sediments. Deeper underplating of sediments beneath the apex of the inner wedge is inferred from seismic imaging [*Collot et al.*, 2008].

Pliocene marine terraces exposed at an elevation of 200–300 m above sea level imply recent coastal uplift in front of the Carnegie Ridge [*De Vries*, 1988; *Pedoja et al*., 2006]. To the north, the morphology of the margin and the drainage pattern of the coastal area support active subsidence [*Dumont et al*., 2006]. Nevertheless, sediment truncated at the seafloor reflects a broad uplift possibly associated with sediment underplating, or cumulative and permanent deformation associated with repeated interplate earthquakes [*Collot et al*., 2008]. This uplift coincides with the basal tectonic erosion of the outer margin wedge, supported by a steep surface slope and the trenchward tilt of the seaward part of the fore-arc basin [*Collot et al*., 2008].

From the Gulf of Guayaquil to Colombia, the fore arc consists of the North Andean block which was accreted to the Brazilian continental craton during the Cretaceous (Figure 1) [*Jaillard et al*., 1997]. These terranes are composed of tholeitic and andesitic basalts, with pillow lavas associated with siliceous sediments [e.g., *Cediel et al*., 2003]. Mafic to ultramafic rocks outcrop in Colombia and Ecuador [*Kerr et al*., 1997; *Lapierre et al*., 2000] and on the Gorgona Island located 60 km offshore the Colombian coast ~300 km north of Esmeraldas [*Révillon et al*., 2000] (Figure 1). In Ecuador, the Piñon Formation, interpreted as an oceanic plateau basement, is overlain by intraoceanic volcanic arc series, such as the Cayo formation [e.g., *Jaillard et al*., 1995; *Reynaud et al*., 1999]. The oceanic plateau sequence described in northwestern coastal Ecuador (Pedernales unit) [*Mamberti et al*., 2003] shares geochemical affinities with Gorgona rocks as well as with the 92–86 Ma Caribbean-Colombian Oceanic Plateau (Figure 1). This suggests that the Pedernales unit belongs to the Late Cretaceous Caribbean-Colombian Oceanic Plateau [*Mamberti et al*., 2003]. The North Andean block behaves as an independent block with respect to the craton, which is drifting in a N35°E direction, parallel to the margin, at 7.3 ± 2.7 mm/yr [*Nocquet et al*., 2009; *Trenkamp et al*., 2002] to the Northeast (Figure 1).

Various observations indicating that the plate interface is highly coupled north of the latitude of the Carnegie ridge include the following: (1) GPS data showing that the margin undergoes significant shortening of ~5 mm/yr perpendicular to the trench axis [*Nocquet et al*., 2009; *White et al*., 2003]; (2) the sequence of four major great subduction earthquakes which ruptured the margin during the twentieth century [*Kanamori and McNally*, 1982; *Kelleher*, 1972; *Mendoza and Dewey*, 1984].

The 1906 earthquake is the seventh largest recorded earthquake on Earth. With an estimated magnitude of 8.8 and a 500–600 km long rupture zone [*Kelleher*, 1972], it generated a tsunami which devastated the coast at the Colombia-Ecuador border. This area was ruptured again from south to north by a sequence of three earthquakes in 1942 ($M_w = 7.8$), 1958 ($M_w = 7.7$), and 1979 ($M_w = 8.2$) (Figure 1). The fact that each rupture of these three more recent events initiated where the previous one ended and propagated from south to north, indicates the presence of discrete asperities separated by weak zones acting as seismic barriers to rupture propagation as defined by *Kanamori and McNally* [1982] and *Beck and Ruff* [1984]. The 1942, 1958, or 1979 earthquake represents the failure of one asperity, which stops in the adjacent weak zone. On the contrary, the 1906 earthquake represents the failure of three asperities, and consequently involves much larger long-strike length and slip [*Kanamori and McNally*, 1982]. Based on seismic reflection data, *Collot et al*. [2004] suggested that these barriers coincide with transverse faults of the margin.

Downdip, the rupture of these three earthquakes appears to have reached ~30 km depth [*Beck and Ruff*, 1984; *Kanamori and McNally*, 1982]. This is in good agreement with results of recent studies on the interseismic microseismic activity [*Manchuel et al*., 2011]. Updip, whereas the rupture of the 1942 and 1979 earthquakes reached the trench, the rupture of the 1958 earthquake ended ~40 km landward of the trench [*Beck and Ruff*, 1984; *Kanamori and McNally*, 1982] possibly because the rupture propagated along a splay fault [*Collot et al*., 2004] (Figure 1).

Although these three events ruptured the same area of the plate boundary overall, they released together only a small fraction of the energy of the 1906 earthquake [*White et al*., 2003] leading to the conclusion that a similar giant earthquake could occur in the area in the near future [e.g., *Papadimitriou*, 1993].

2.2. Rupture of 1958 Earthquake

Beck and Ruff [1984] using long-period seismometers available in 1958 were able to determine the source time function of the 1958 earthquake using the assumptions that the source time function constrained the size of the asperity and length of the rupture along strike, and that the width of the rupture in the dip direction is only constrained by aftershock locations. The aftershocks which occurred within 3 months of the main shock beneath the overriding plate [*Beck and Ruff*, 1984] were distributed in an area extending

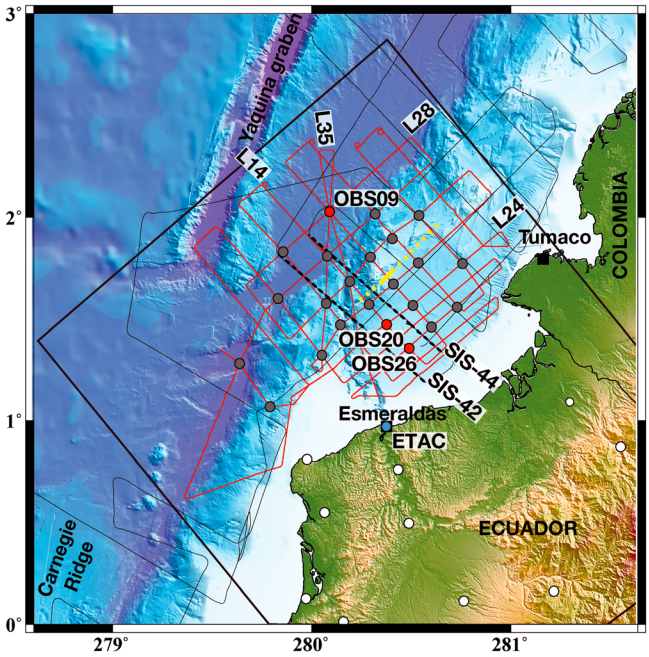

Figure 2. Bathymetry and topography of the margin of North Ecuador and South Colombia. Bathymetric chart is from *Collot et al.* [2009] and *Michaud et al.* [2006]. Location of OBS (gray circles), land seismometers (white circles) and shooting lines (continuous red lines) of the Esmeraldas experiment (2005). OBS (red circles), station ETAC, and profiles corresponding to the seismic sections shown in Figure 2 are labeled. Thin black lines represents location of profiles collected during the Sisteur experiment [*Collot et al.*, 2002, 2004, 2008]. Thick dashed lines show the location of SIS-42 and SIS-44 discussed in the text. A black line outlines the box used for the tomographic inversion.

seaward to near the deformation front for the 1942 and 1979 earthquakes, but they only extend to 40 km from the trench for the 1958 event (Figure 1). The E-W aftershock positions were poorly controlled due to a poor azimuthal worldwide station distribution, whereas the N-S distribution is better defined due to the high number of arrivals recorded at stations in North America [*Beck and Ruff*, 1984].

Even with the significant uncertainties in E-W epicentral location of the aftershocks, it is clear that the coseismic slip of the 1979 and 1942 earthquakes propagated further seaward than the 1958 earthquake (Figure 1). Multichannel seismic line SIS-44 (Figure 2) shot across the north Ecuador–south Colombia oceanic margin imaged a crustal splay fault which coincides reasonably well with the seaward limit of the rupture zone of the 1958 event [*Collot et al.*, 2004, 2008]. The splay fault separates high velocity (5.0–6.6 km/s) inner wedge basement rocks, which belong to the accreted Gorgona oceanic terranes, from lower velocity (3.5–5.0 km/s) outer wedge rocks [*Collot et al.*, 2004, 2008, this study].

The 1958 earthquake was tsunamigenic, implying basement rise or earthquake-induced offshore sediment instability and slumping [*Tsuji et al.*, 1995]. According to a paleoseismic study done in the area, it appears that there are no large turbiditic deposits which can be related to $M < 8.2$ earthquakes [*Ratzov et al.*, 2010], meaning that sediment slumping is not likely the cause of the tsunami recorded in 1958 [e.g., *Ioualalen et al.*, 2011] and implying basement uplift as the most likely mechanism.

Subduction earthquakes occur along shallow-dipping plate interfaces, and the subsequent displacement in an elastic model is predominantly horizontal. Nevertheless, several mechanisms have been proposed to explain tsunami generation: Either the rupture propagates along the interplate all the way to the trench, implying deformation and uplift of the low rigidity accretionary prism [e.g., *Ma*, 2012], or the rupture propagates along a secondary more steeply dipping fault, called splay fault, whose slope enhances vertical displacement [e.g., *Moore et al.*, 2007].

2.3. Previous Geophysical Cruises

Our group has previously conducted several seismic experiments along the south Colombia-Ecuador convergent margin which provide a unique set of high-quality, 2-D wide-angle reflection/refraction, multichannel seismic profiles (SISTEUR-2000 and SALIERI-2001 surveys, Figure 2) [*Collot et al.*, 2002; *Flueh et al.*, 2001] and high-resolution bathymetry (AMADEUS-2005).

3. Data Acquisition and Processing

3.1. The Esmeraldas 3-D Active Source Tomography Experiment

In 2005, we conducted a combined onshore and offshore 3-D seismic experiment named Esmeraldas (from the nearest Ecuadorian town) using ocean bottom seismometers (OBS) and land stations with the aim of

providing information on the spatial variation of the upper and lower plate over the 1958 earthquake rupture zone and the transition to the 1979 and 1942 earthquake rupture zones. The major questions addressed by this study are the following: What is the along strike extend of the outer margin wedge? What is the precise location and along-strike extension of the low-velocity zone inferred from 2-D wide-angle seismic experiments [*Gailler et al*., 2007; *Collot et al*., 2008; *Agudelo et al*., 2009]? What is the structural nature of the seismic barrier between the 1958 and 1979 rupture zones? Our ultimate goal is to discern if any correlation exists between the extension of the rupture area and the elastic properties around the interplate boundary along the seismogenic zone.

3.2. Data Acquisition

The acquisition grid of the Esmeraldas experiment (Figure 2) consists mainly of a set of 10 trench-parallel profiles and 10 trench-perpendicular profiles, plus two oblique ones. These seismic lines are ~200 km long, have a mean separation of ~15 km, and cover a surface of 33,600 km^2 of the margin from the subducting plate to the continental shelf. The French R/V *Atalante* (Ifremer) deployed 23 four-component OBS [*Hello et al*., 2006], one at each node of this grid. A total of ~18,500 shots were fired along ~2900 km of profiles. The seismic source consisted of an untuned array of eight air guns of 16 L each (128 L for the whole array) fired every 150 m. In addition, 14 of 31 land stations deployed across Ecuador for seismological recording also recorded the marine seismic shots [*García Cano*, 2009].

3.3. Data Processing and First-Order Results

A total ~1200 inline and offline seismic record sections were extracted from continuous recordings of OBS and land stations. We took advantage of having shot twice above each OBS along two perpendicular shooting lines to determine accurately the location of the sensor on the sea bottom and the orientation of the horizontal components, allowing rotation of the data into radial and transverse components [*Manchuel et al*., 2011; *Nakamura et al*., 1987], using the traveltimes and polarization of the direct wave arrivals.

On most OBS, the signal-to-noise ratio is high and arrivals can be seen at source-receiver offset up to 145 km (Figure 3). For land station record sections (Figure 3d), which have a much lower signal-to-noise ratio than the OBS data, we used a frequency-dependent phase coherency filter [*Schimmel and Gallart*, 2007] to enhance the signal at large offsets (up to 195 km) and to improve picking of first arrivals.

Refracted phases which have apparent velocities consistent with wave propagation through sedimentary rocks ($<$ 4 km/s) and crustal layers (5–7 km/s) can be seen in all OBS sections, and phases having apparent mantle-like velocities higher than 8 km/s can be seen on both OBS and land stations (Figure 3). A shadow zone, which could be due to the presence of a low-velocity zone, is observed on both OBS and land stations at similar source-receiver offset of 40–60 km (Figure 3).

4. Three-Dimensional Tomographic Inversion

4.1. Arrival-Time Picks From OBS and Land Stations

A total of ~197,000 first arrivals were picked manually on OBS and land stations. Picking error, which were based on lateral phase coherency, ranges from 20 ms for near-field arrivals to a maximum error of 100 ms for the less coherent arrivals at farthest offset. We paid special attention to consistency between OBS and land station picking and error assignments, and we also checked consistency of traveltime picks at the crossing point of inline and offline record sections (Figure 3) [*García Cano*, 2009].

4.2. Initial Model

A rectangular box was defined to create the grid to perform the tomographic inversion (Figures 1 and 2). Its sides are parallel to the shot lines, encompassing all the shots, OBS, and land stations.

The dimensions of the inversion box are 332 km × 254 km × 65 km and the origin of the grid was placed at the northwestern corner. The grid comprises cells of 0.5 km × 0.5 km × 0.5 km for the forward problem and 2 km × 2 km × 0.5 km for the inverse problem.

We used the regularized inversion algorithm FAST, which calculates traveltimes using a finite difference solution to the Eikonal equation [*Zelt and Barton*, 1998; *Vidale*, 1990], to derive the 3-D velocity structure.

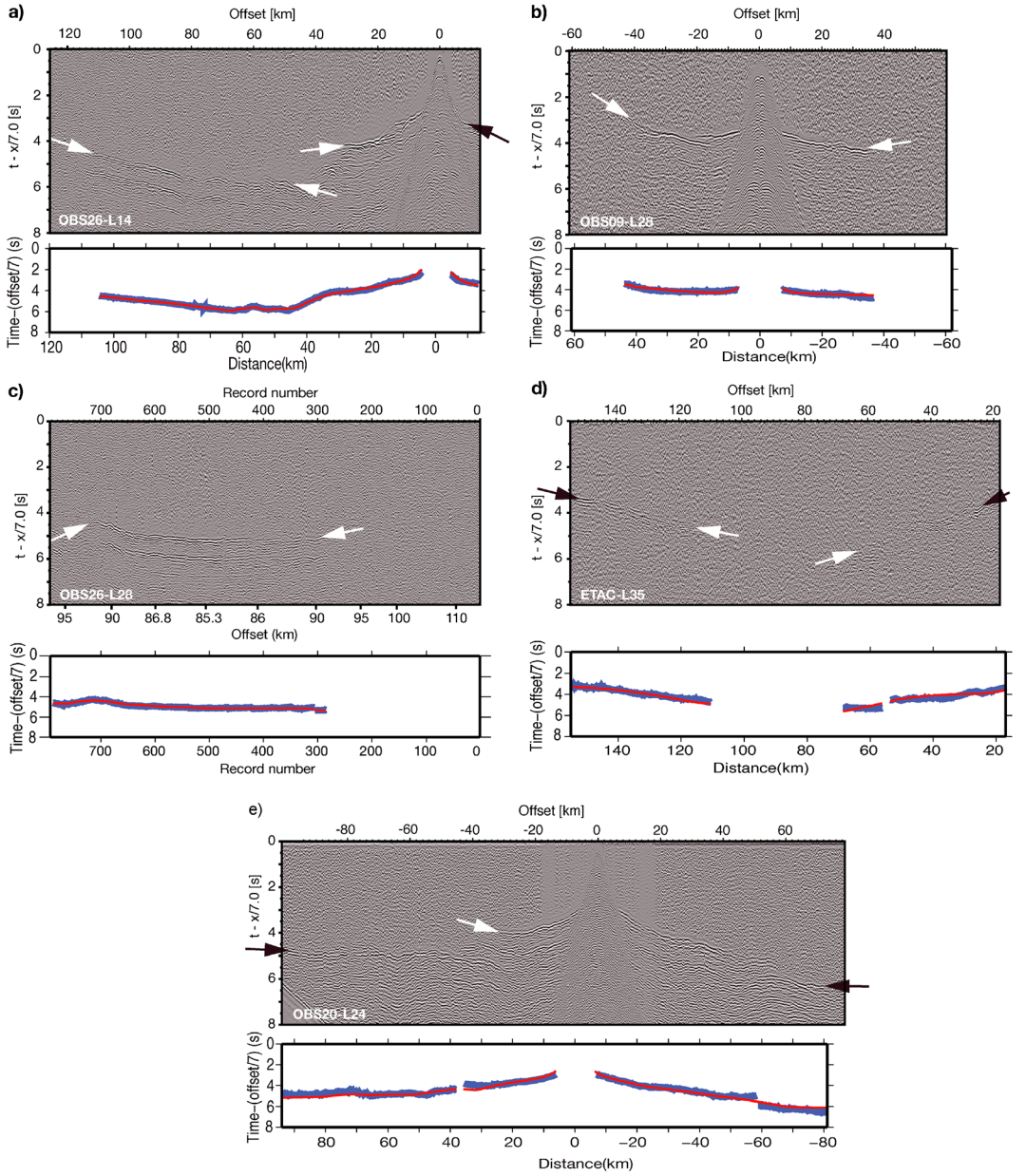

Figure 3. Example of seismic record sections used in this study. Beneath each record section a plot of synthetic (red) and observed (blue) traveltimes is shown: (a) profile 14 recorded by inline OBS 26; (b) profile 28 recorded by OBS 09; (c) profile 28 recorded by offline OBS 26; (d) profile 35 recorded by land seismometer ETAC; and (e) profile 24 recorded by OBS 20 (see Figure 2 for location of OBS and profiles). A predictive deconvolution, a 3 to 12 Hz minimum phase Butterworth filter and an automatic gain control were applied to the OBS record sections. A frequency-dependent phase coherency filter [*Schimmel and Gallart*, 2007] was applied to land-stations record sections. Arrows indicate first arrivals used in the inversion. The reduction velocity is 7.0 km/s. Shadow zones exist between 40 and 50 km offset on sections OBS26-L14 and OBS20-L24.

In the initial model, the topography of the seafloor derived from compilation of swath bathymetry data [*Collot et al*., 2009; *Michaud et al*., 2006], smoothed and interpolated at 0.5 km interval. In order to determine the effect of the initial model on the inversion result, we tested two different starting models: Model 1 has the velocity-depth characteristics of an oceanic crust with a strong vertical velocity gradient in the crust and the Moho 5 km deep below sea bottom whereas model 2 is characterized by a weaker gradient and a Moho 18 km

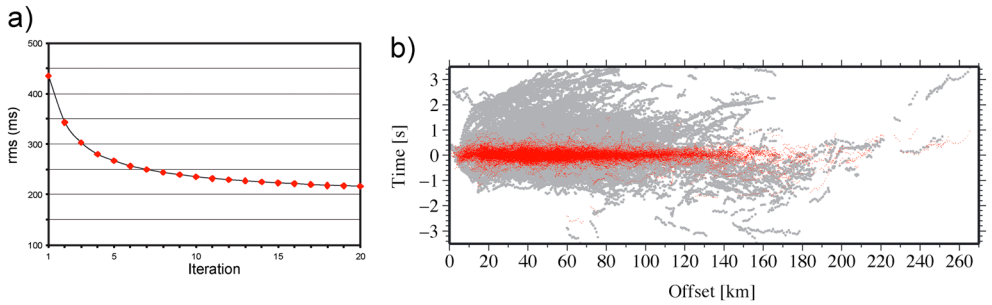

Figure 4. Evolution of misfit during the inversion. (a) Variation of the RMS with successive iterations for all the traveltimes. The final RMS is 217 ms. (b) Traveltime residuals versus offset diagram in gray for the starting model and in red for the final model. The 63% of residuals are lower than 0.1 s whereas 5% are higher than 0.5 s. Higher residuals are observed for far offset fan profiles on OBS and some land stations (0.08% of outliers).

deep below sea bottom (supporting information Figure S1). Final models obtained using either model 1 or 2 as starting model exhibit no significant difference (Figure S1), but in the following, we will present results based on model 2 which yielded a slightly lower RMS traveltime misfit (Figure 4).

4.3. Three-Dimensional Tomographic Final Inversion and Resolution Analysis

Tests were made to determine a range of free parameters which control the effect of vertical versus horizontal model roughness (Sz) or the regularization parameter (λ). These parameters were determined by trial and error, to get the best fit between calculated and observed traveltimes and the smoothest final model. Finally, the chosen values were Sz = 0.5 and λ = 20%. Our preferred final model was obtained through 20 iterations and first arrivals were fit with a misfit (RMS) of 217 ms (Figure 4). The normalized chi-squared is as high as 10.2 indicating that the traveltime data are not fit to their nominal picking uncertainty (20 ms for near-field arrivals to a maximum of 100 ms for farthest offset). This is coherent with the 217 ms RMS and can be explained by a few mispicked first arrivals on traces with low signal-to-noise although we eliminated some picks with large residuals in our preliminary inversions. A more likely explanation for the high residuals is the complexity of 3-D velocity variations in the study area, which is hardly taken into account with a smooth tomographic model. Vertical and horizontal slices (Figures 5–7) were extracted from the 3-D *P* wave velocity model for visualization.

Checkerboard tests have been performed to assess data resolution (Figure 8). We added a ±8% velocity perturbation to our best final velocity model and generated traveltimes using our study source-receiver geometry. Gaussian noise is added to these traveltimes to create a synthetic data set. Using our best final velocity model as an initial model, we then look at the ability of the inversion to recover the input anomaly pattern. Where the geometry and amplitude of the anomaly pattern are recovered, the velocity model is considered well resolved at the length scale of the anomalies. Several tests were done for different sizes of anomaly. Figure 8 highlights checkerboard test results for anomalies having horizontal dimension of 20 km × 20 km or 30 km × 30 km and thickness of 5 km and 10 km.

Horizontally, we can resolve the geometry and amplitude of structures located below the OBS network quite well for structures having dimensions of 20 km × 20 km between 5 km and 10 km depth. Between 10 and 15 km depth, resolution is restricted to the center of the network and anomalies start to become blurred (Figure 8a). Below 15 km, we can only resolve structures larger than 30 km × 30 km in the center of the model (Figure 8b). Vertically, we resolve in the center of the model 5 km thick structures between 10 and 20 km depth and only 10 km thick structures outside of this area (Figures 8c and 8d).

Note that the ray coverage related to onshore stations provides additional constraints on the velocity structure at depth between the coast and the offshore network (see, for example, checkerboard test at 12.5 km depth, Figures 8b and S2). Vertical and horizontal slices (Figures 5–7) were extracted from the 3-D *P* wave velocity model for visualization.

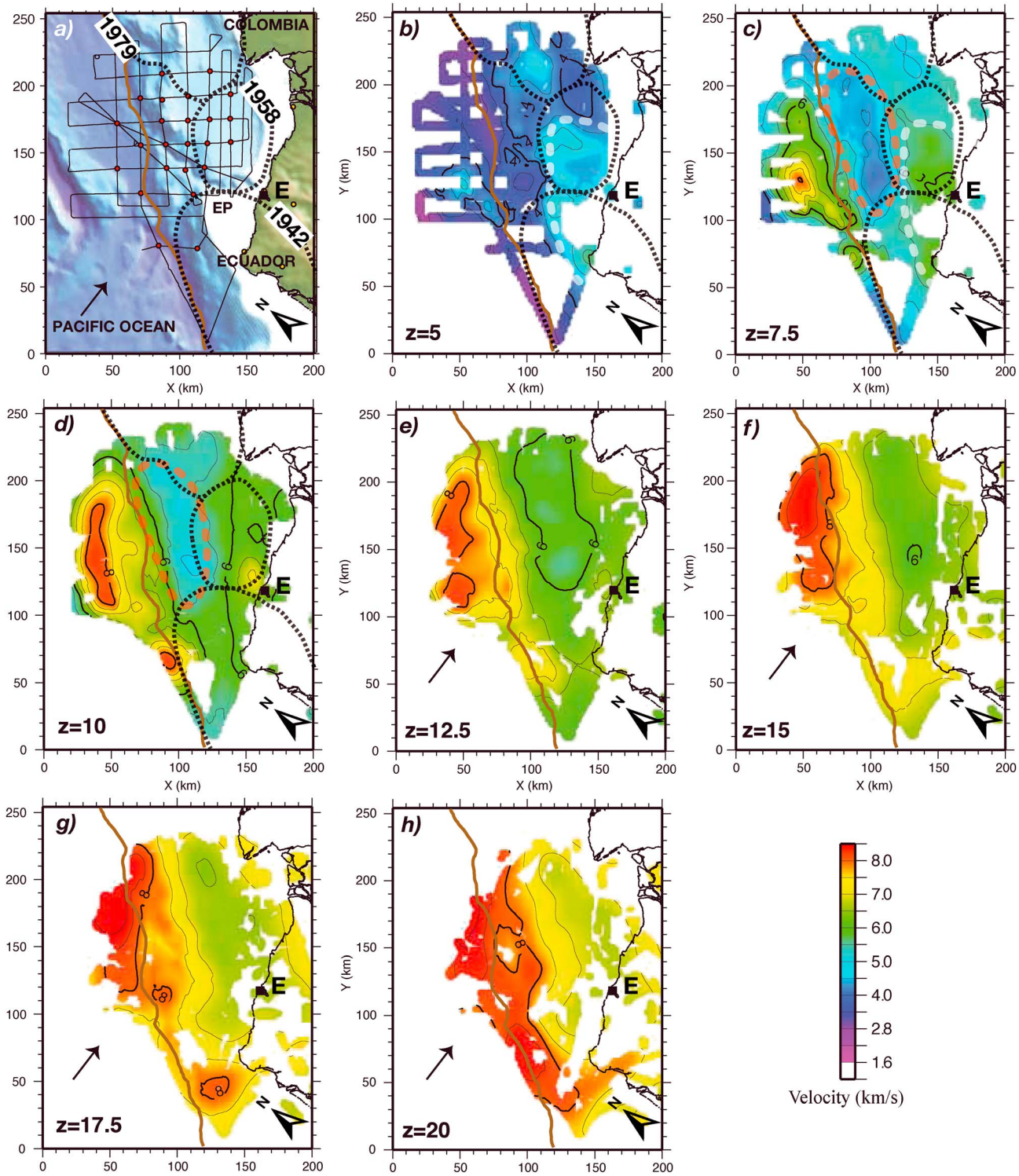

Figure 5. (a) Bathymetry and topography. Thin lines are shooting lines, red circles are OBS. The thick brown line is the trench axis. Thick dashed lines outline the rupture zone of the 1942, 1958, and 1979 earthquakes. E is the city of Esmeraldas and EP the Esmeraldas promontory. (b to h) Horizontal sections made at different depth of our final velocity model. The depth of these horizontal sections and the north are indicated in each inset. Thick lines are every 2 km/s velocity contours and thin line for intermediate contours. Areas uncovered by rays appear in white. The coast appears in black, the brown line marks the axis of the trench, and the thick black dashed lines outline the rupture zone of the 1942, 1958, and 1979 earthquakes. The black arrow represents the convergence direction. The thick white dashed line outlined the basement uplift observed offshore Esmeraldas (Figures 5b and 5c), and the thick red dashed line outlined the low vertical velocity gradient outer wedge (Figures 5c and 5d).

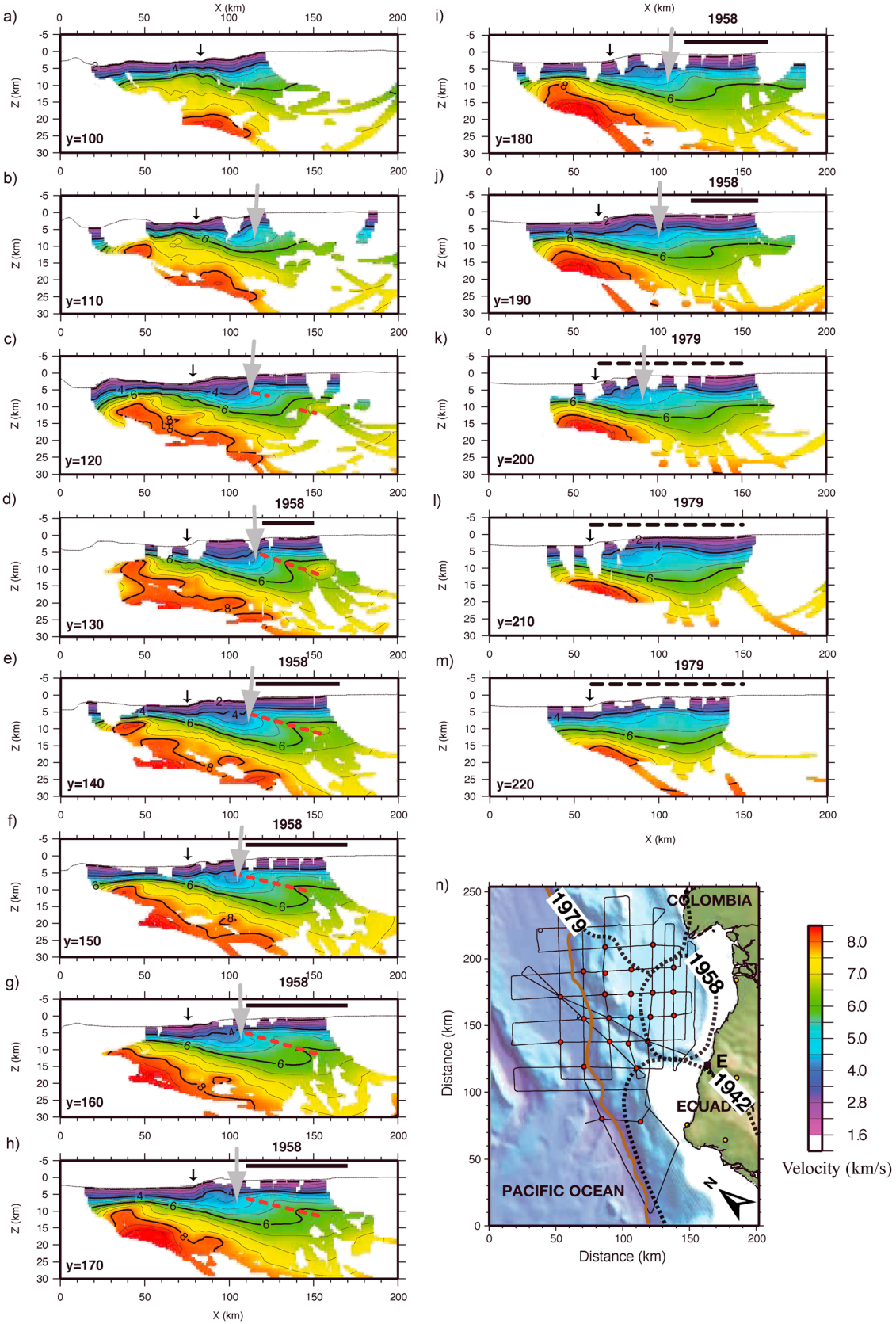

Figure 6

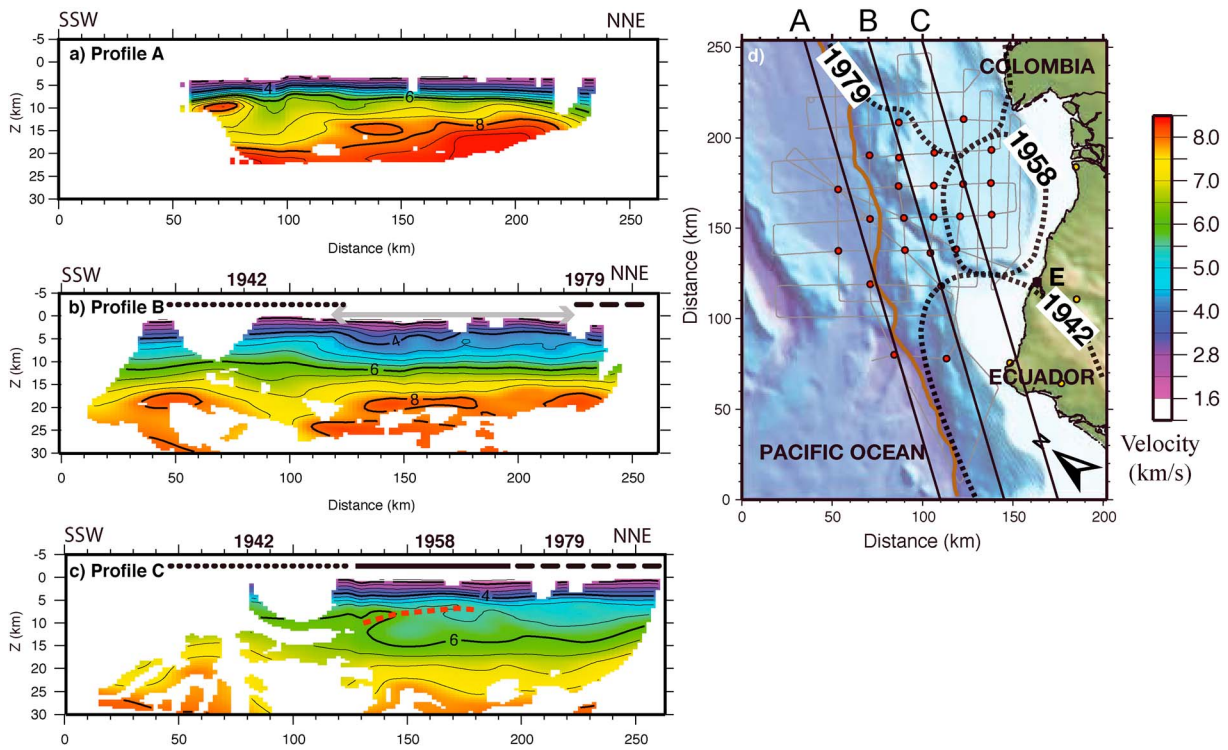

Figure 7. (a–c) Vertical sections made through our final velocity model along three profiles A, B, and C, parallel to the trench. Locations of profiles are indicated in Figure 7d. Velocity contours and mask are the same than in Figure 5. Horizontal gray arrow marks the extent of the low vertical velocity gradient outer wedge. The red dashed line outlines the top of the deep low-velocity zone. Dashed and continuous black lines mark the extent of the rupture zone of 1942, 1958, and 1979 earthquakes. (d) Bathymetry and topography. Same as Figure 5a.

4.4. Three-Dimensional Velocity Structures

According to *Gailler et al*. [2007], the top of the acoustic basement, which constitutes the base of the recent sedimentary basins along multichannel seismic (MCS) profile SIS-44 (Figure 2), corresponds to velocities ranging from 3.5 to 4.0 km/s. Along MCS line SIS-42 (Figure 2), the acoustic basement, interpreted to have originated as an oceanic plateau or volcanic arc [*Marcaillou et al*., 2008], coincides with seismic velocities ranging from 3.5 to 4.5 km/s (Figure 9). This is also consistent with *Vp* estimated to be ≥ 4 km/s in the upper part of the acoustic basement [*Collot et al*., 2008]. According to these interpretations, the sedimentary thickness ranges from 1.3 to 2.0 km on top of the oceanic crust westward from the trench. On the shelf, the sedimentary thickness ranges from 3.0 km beneath the bathymetric high located offshore of the town of Esmeraldas ($Y = 140$–160, Figures 6e–6g) to 4.0 km to the northeast. This bathymetric high is clearly seen as high-velocity anomalies on horizontal slices at 5.0 and 7.5 km depth (outlined in Figures 5b and 5c) and denotes a ~1 km uplift of the acoustic basement offshore Esmeraldas which coincides partly with the submarine Esmeraldas promontory (Figure 5a).

The deepening of the subducting plate toward the southeast is well imaged by the observed deepening of the 7.5–8.0 km/s isovelocity contours, which are representative of upper-mantle velocities (Figures 5–7). The smoother and better constrained 7.5 km/s isovelocity contour, which mimics the 8.0 km/s isovelocity contour, shows that the dip of the Moho beneath the fore arc west of the trench is $10 \pm 0.5°$ in the well-constrained part of the model (Figure 6). Assuming the oceanic crust is bounded by the 4.0 km/s and 7.5 km/s isovelocity

Figure 6. (a–m) Vertical sections made through our final velocity model perpendicular to the trench. Locations of profiles are indicated in inset. Velocity contours and mask are the same than in Figure 5. The vertical black arrow indicates the position of the trench, the vertical gray arrow marks the inner limit of the low vertical velocity gradient outer wedge. The red dashed line outlines the top of the low-velocity zone. The horizontal thick black line shows the extension of the rupture of the 1958 event, and the horizontal thick dashed line the extension of the rupture of the 1979 event [*Beck and Ruff*, 1984; *Kanamori and McNally*, 1982]. (n) Same as Figure 5a.

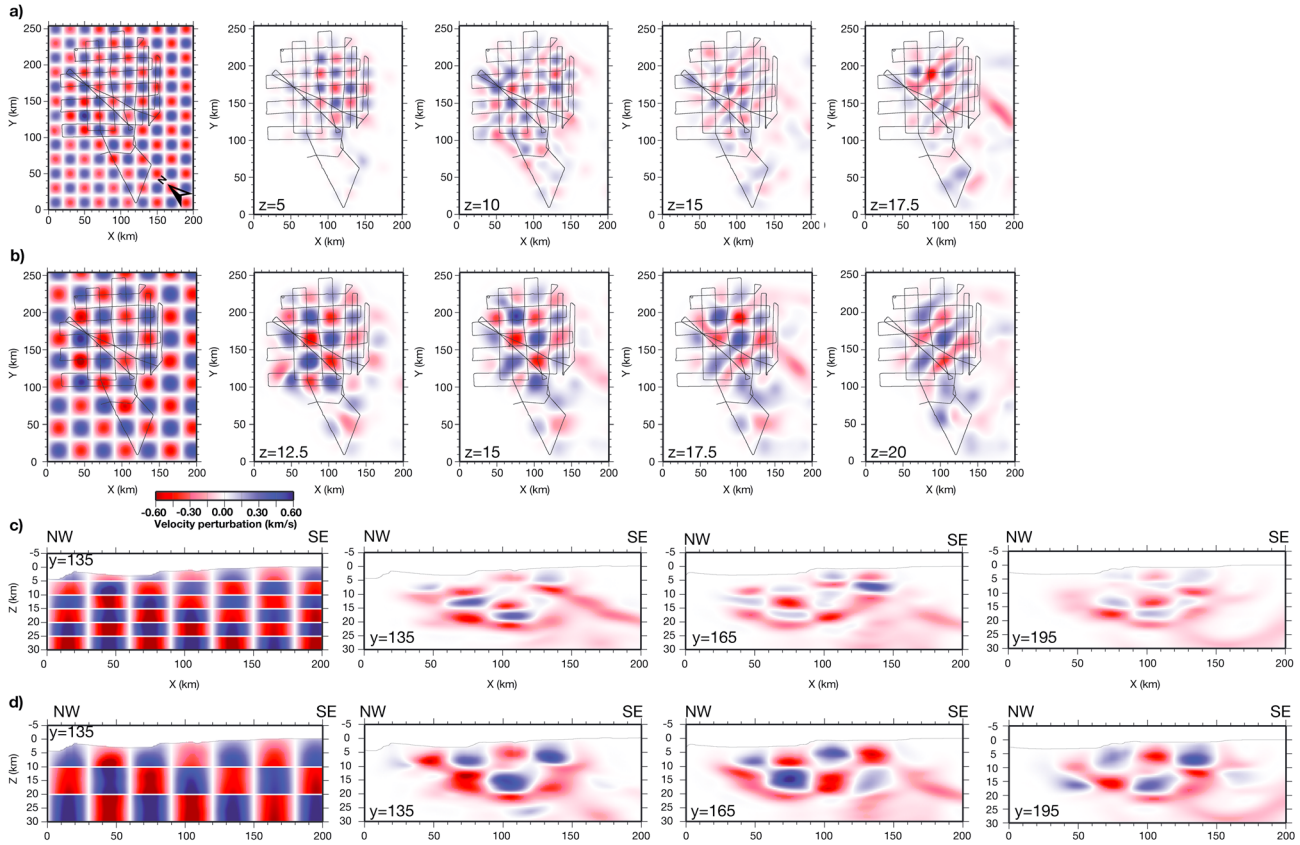

Figure 8. Results of the checkerboard tests for (a) 20 × 20 km velocity anomalies, (b) 30 × 30 km velocity anomalies, (c) 30 × 30 × 5 km velocity anomalies, and (d) 30 × 30 × 10 km velocity anomalies. This test shows that the horizontal resolution of our model is ~20 km down to 12 km and ~30 km for the deeper part. The vertical resolution is ~5 km in the center part of the network.

contours at its top and base, respectively, we observe a thinning of the subducting crust toward the north from ~9.0 km (at distance = 100 km) to ~4.5 km (at distance = 200 km) (Figure 7a) which is consistent with moving away from the Carnegie ridge and consequently from the influence of the Galapagos hotspot [e.g., *Sallarés and Charvis*, 2003].

A positive velocity anomaly observed on the oceanic crust prior to the trench at $X = 40–50$ on the $Z = 7.5$ km horizontal slice (Figure 5c) seems to show a Moho uplift and the presence of thin oceanic crust. At the surface, it corresponds to the eastern flank of the Yaquina graben. The western flank of this structure is not well resolved, and we do not image its extension beneath the center of the graben.

We see no evidence for phases reflected from the Moho or refracted within the upper mantle of the upper plate. However, two dominant features come out on vertical and horizontal slices: a low vertical velocity gradient outer margin wedge and a low-velocity zone located in the upper plate above the interplate contact (Figures 5–7).

4.5. A Low Vertical Velocity Gradient Outer Margin Wedge

A low vertical velocity gradient area is imaged on horizontal (outlined in Figures 5c and 5d) and vertical slices (Figures 6b–6k and 7b) and forms the trench side part of the margin wedge. On vertical slices, for example, at $y = 140$ km (Figure 10), this outer margin wedge can be seen from the trench to $x = 120$ km and is characterized by low *P* wave velocities of 3.5–5.0 km/s. The striking feature of this outer margin wedge is an average vertical velocity gradient of 0.24 km/s/km, which in place is as low as 0.13 km/s/km, compared with an average vertical velocity gradient of the uppermost basement greater than 0.6 km/s/km. The extension along strike of the low-gradient zone is imaged on the horizontal slices; at 7.5 km and at 10 km depth

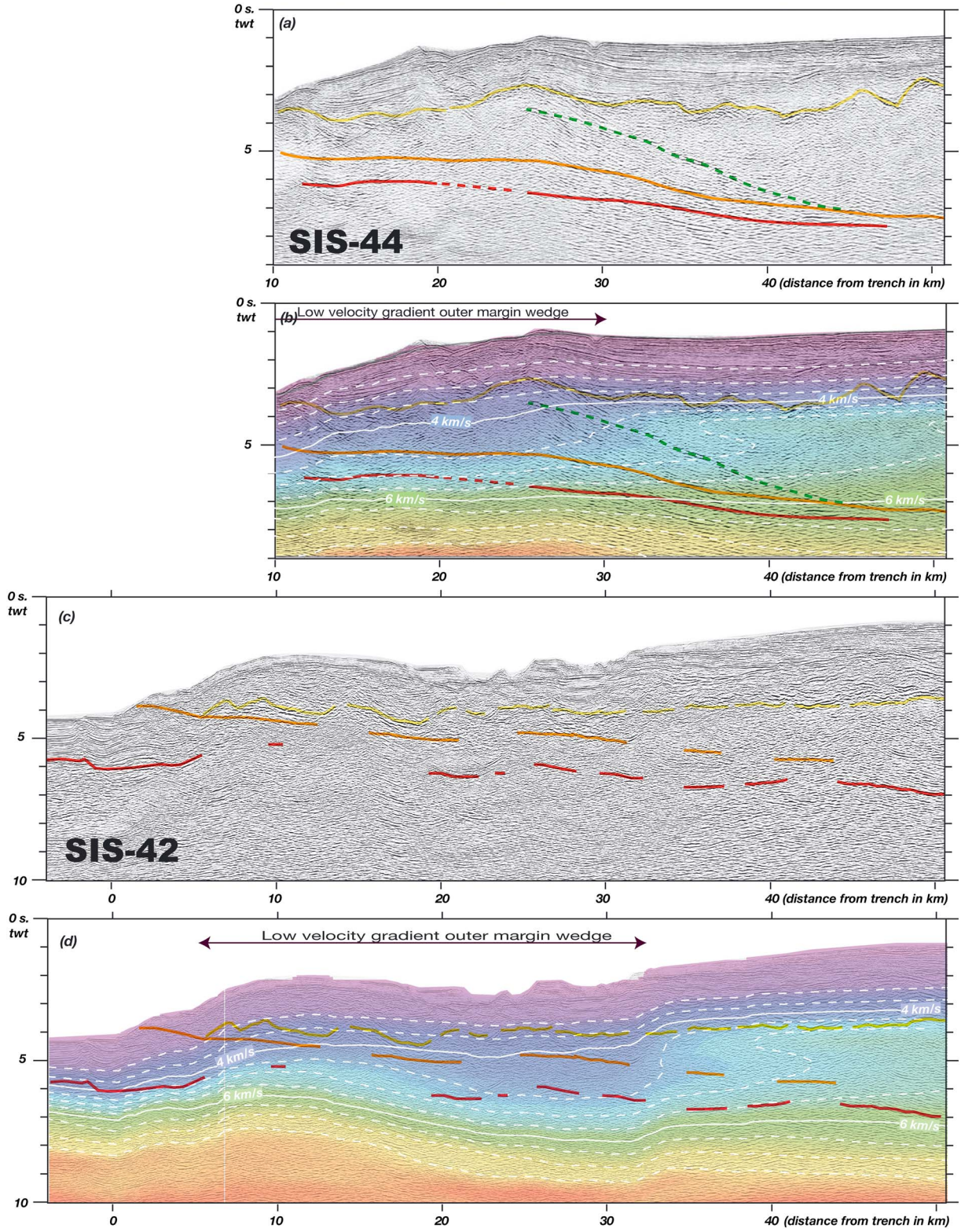

Figure 9. (a) Multichannel seismic (MCS) line SIS-44. (b) Superposition of MCS SIS-44 and the tomographic velocities from our final model converted to two-way traveltime. Yellow, green, orange, and red lines highlight, respectively, the upper plate basement, the splay fault, the décollement, and the top of the downgoing oceanic crust as interpreted from the MCS data [after *Collot et al.*, 2004]. The upper plate basement velocity corresponds to tomographic velocity contour of ~3.5 km/s in the outer margin wedge and ~4.5 km/s in the inner margin wedge. (c) Same as Figure 9a for profile SIS-42. (d) Same as Figure 9b for profile SIS-42.

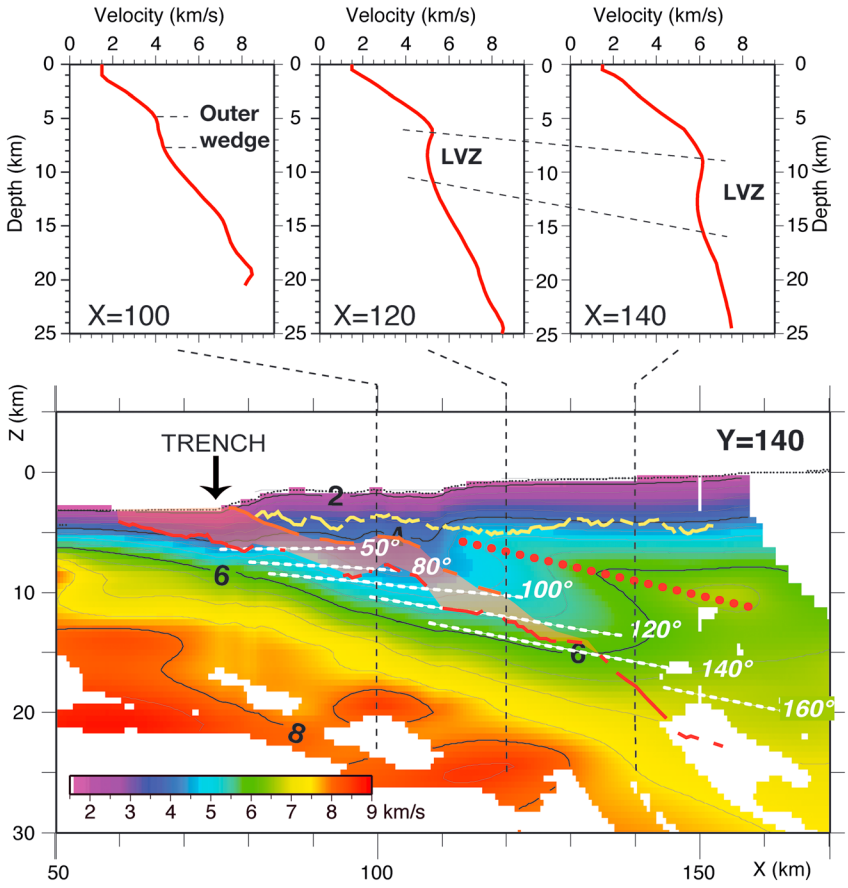

Figure 10. Interpretation of vertical section at $Y = 140$ (Figure 6). Velocity versus depth curves at $X = 100$, 120, and 140 exhibit the low-velocity gradient outer wedge ($X = 100$) and the low-velocity zone in the margin. Superimposed on the vertical section: in yellow the basement, in orange the décollement and in red the top of the subducting plate, as interpreted in MCS line SIS-42 (Figure 9) and converted into depth using our tomographic velocity model. Note that the velocity in the subduction channel, located between the décollement and the top of the lower plate, is not properly constrained in our model, and consequently, the thickness of the channel is larger than the one inferred in other studies [*Collot et al.*, 2008]. The top of the low-velocity zone is highlighted by a red dotted line. Isotherms in °C are from *Marcaillou et al.* [2006] and *Collot et al.* [2008].

(Figures 5c and 5d) as well as along a line parallel to the trench (Figure 7b), the low-velocity outer margin wedge extends over ~90 km parallel to the trench with a width of 40 km.

4.6. A Low-Velocity Anomaly in the Margin

On the vertical slices between offset of $x = 120$ km to $x = 150$ km, infolding of the 4.5 km/s to 6 km/s isovelocity contours indicate the along-strike continuation of a low-velocity zone in the margin crust (Figures 6c–6h). This low-velocity zone is located between $y = 130$ km and $y = 170$ km at the southeastern side of the offshore network. This is consistent with the shadow zone observed on many of the OBS located on the margin (Figures 3a and 3e). One-dimensional velocity models (Figure 10) extracted from 2-D sections show that *P* wave velocities are ~5.5–6.0 km/s in the low-velocity zone, varying with depth and represent a decrease of 0.35 km/s with respect to the overlying velocity. This low-velocity zone dips southeastward with a similar angle to the subducting plate. Its trench side limit seems to abut the low-velocity outer margin wedge. *Gailler et al.* [2007] has previously inferred such a low-velocity zone from a 2-D tomographic image obtained by using a dense OBS profile located in the center of our tomographic box (coincident with profile SIS-44, Figures 2–9).

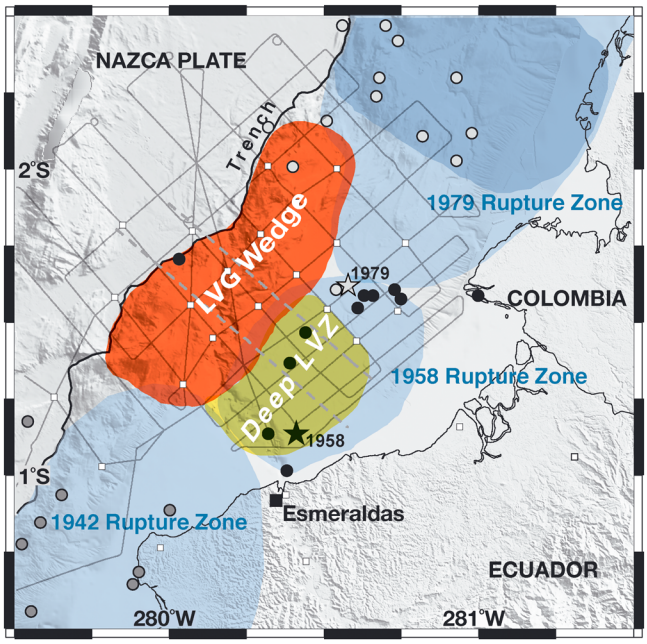

Figure 11. Three-dimensional extension of the low-velocity gradient outer wedge (red), the deep low-velocity zone (yellow) inferred from this study, and the 1942, 1958, and 1979 earthquakes rupture zones (blue). Light blue areas are rupture zones and dark blue circle is the asperity region of 1979 earthquake as defined by *Beck and Ruff* [1984]. The light blue area of the 1979 rupture zone was modified according to our interpretation of the rupture mechanism. Main shocks (stars) and aftershocks (closed circles) of the 1942, 1958, and 1979 earthquakes are defined as in Figure 1. A thick black line underlined the axis of the trench. Gray lines mark seismic shooting tracks and white squares mark ocean bottom and land seismometer positions. Dashed lines mark the location of MCS profiles discussed in the paper.

5. Discussion

Our 3-D velocity model shows the spatial extension of structures seen on previous 2-D geophysical data sets [*Gailler et al.*, 2007; *Collot et al.*, 2004]. Correlating the 3-D extension of these structures with the rupture zone of the 1958 and 1979 subduction earthquakes allows us to infer and discuss the potential role of these structures in the seismic cycle.

5.1. Extension of the Low-Velocity Gradient Outer Margin Wedge and Seismic Implications

At the front of non-accretionnary margins, low *P* wave velocities (3.5–5.0 km/s) observed in the outer margin wedge are usually interpreted to be associated with fracturing, and/or alteration processes which increase the porosity of margin basement rocks [*Christeson et al.*, 1999; *Gailler et al.*, 2007; *Krabbenhoft et al.*, 2004; *Ranero and von Huene*, 2000; *Sallarés and Ranero*, 2005]. The fracturing of the backstop is possibly related to the impact of seamounts which entered the subduction zone [*Collot et al.*, 2008] or to the subduction of the Carnegie Ridge, which affected this area in the past [*Michaud et al.*, 2009]. The fluids expelled during the subduction possibly contribute to fracturing and alteration of the outer wedge [*Ranero et al.*, 2008].

Our data set reveals the extension of the low-velocity gradient outer margin wedge over ~100 km along strike from 1°15′N to ~2°00′N (Figure 11). The outer margin wedge consists of up to 2.5 km of sediments on top of the basement and up to ~4 km of basement rocks at $X = 110$ km (Figure 10). It likely sits on top of the subduction channel as indicated by MCS line SIS-42 [*Marcaillou et al.*, 2008, Figures 6 and 9] but this is not resolved in our tomographic model as the vertical resolution is ~5 km (Figure 8c), and larger than the expected 2–3 km thickness of the subduction channel [*Collot et al.*, 2008]. This wedge coincides with the outer basement high described by *Collot et al.* [2004] and bounds the margin seaward of the 1958 rupture zone (Figures 6d–6j).

Along profile SIS-44 (Figure 9), the outer margin wedge coincides with the toe of the margin and its landward flank is bounded by a splay fault [*Collot et al.*, 2004, 2008]. Along line SIS-42, ~20 km southwest of line SIS-44, the data do not show evidence of a splay fault bounding the outer margin wedge landward (Figure 9).

It has been suggested that highly damaged rocks have an excessive number of branching and bifurcating cracks which give rise to inelastic behavior, enhancing energy dissipation [*Barragan et al.*, 2001]. Consequently the highly faulted outer wedge probably results in larger energy dissipation during failure [*Kanamori and Brodsky*, 2004]. We therefore propose that the 1958 rupture propagated along the main interplate megathrust. The low seismic velocities, highly fractured, outer wedge is mechanically similar to the accretionary prism in other subduction zones. This low rigidity outer wedge dissipated most of the seismic energy, which explains the lack of coseismic slip at the base of the outer wedge observed during the 1958 event. Under this assumption, the seismic rupture propagation leads to widespread failure and

large coseismic seafloor uplift of the low rigidity outer wedge and may account for the tsunami generation [*Ma*, 2012].

Our 3-D tomographic image constrains the 3-D extension of this low-velocity gradient outer margin wedge (Figures 5–7) which extends northeastward seaward of the southern part of the 1979 rupture zone (Figures 6k–11). *Beck and Ruff* [1984] modeled the 1979 seismic rupture as a succession of three ruptures moving from south to north. The first rupture was 56 km along strike and ended at the northern tip of the low-velocity gradient outer wedge. The updip-downdip width of this first rupture of the 1979 earthquake is poorly constrained by seismograms [*Beck and Ruff*, 1984], but according to the distribution of aftershocks in this area (Figure 11), it might have behaved like the rupture in the 1958 earthquake, which ruptured the interplate boundary to the outer margin wedge and then propagated northward in a second rupture which reached the trench.

5.2. Extension of the Low-Velocity Zone at Depth

The low-velocity zone (LVZ) observed in our model is mainly located above the interplate boundary but it likely includes the subduction channel at its base (Figure 9). It is up to 5 km thick and extends from 5 to 15 km depth (Figure 6 and 9). The minimum velocity in the LVZ (i.e., ~5.5–6.0 km/s) is ~5–6% lower than the velocity at the top of the LVZ.

Such low seismic velocity layers have been imaged in several places along convergent margins where they are frequently interpreted to result from fracturing of the upper plate because of high fluid pressure in the subduction channel: e.g., the Nicaragua and Costa Rica margin [*Christeson et al*., 1999; *Walther et al*., 2000], the North Chile margin [*Sallarés and Ranero*, 2005], or the Cascadia margin [*Tréhu et al*., 1994; *Gerdom et al*., 2000; *Calkins et al*., 2011]. Nevertheless, such a decrease of seismic velocity with depth could also be related to different physical or chemical causes, including a change in the composition, mineralogy, or porosity of igneous or sedimentary rocks. Some other interpretations are proposed in the Cascadia margin where low seismic velocities are related to material underplated at the base of the upper plate [*Calvert et al*., 2011; *Tréhu et al*., 2012].

We will therefore discuss these two major hypotheses: either the observed LVZ is related to the alteration and fracturing of the rocks of the upper plate or to material underplated at the base of the upper plate.

The basement of the margin of Ecuador is composed of mafic to ultramafic rocks, belonging to the Gorgona province, a Cretaceous oceanic terrane accreted to the margin [*Lapierre et al*., 2000]. These rocks are likely present along the whole margin as supported by high seismic velocities described along the margin from Salinas to the Colombian border [*Gailler*, 2005; *Gailler et al*., 2007]. In northwestern Ecuador, the Pedernales unit consists of volcanic and plutonic rocks with a high MgO contain (up to 25% MgO in the parent liquid after *Révillon et al*. [2000]). They were emplaced in an oceanic plateau setting and range from dunites (olivine cumulates at the base of the series) to gabbros and basalts [*Révillon et al*., 2000; *Mamberti et al*., 2003].

Seismic velocities in mafic and ultramafic rocks are strongly influenced by their water content. Velocity decreases with increasing water content [*Carlson*, 2003; *Carlson and Miller*, 2003; *Hacker and Abers*, 2004] because of changes in the mineralogy such as the serpentinization of olivine but also because the hydration of ferromagnesian minerals, which are abundant in mafic rocks (hydration of pyroxenes in amphiboles). The depth of the LVZ, from 5 to 15 km, corresponds to lithostatic pressure of 0.2 to 0.5 GPa and, according to available heat flow modeling, to a temperature ranging from ~50°C to ~140°C [*Marcaillou et al*., 2006, 2008]. According to *Hacker et al*. [2003], these values of pressure and temperature correspond to zeolite to prehnite-pumpellyite metamorphic facies [*Hacker et al*., 2003, Figure 1]. Using the method of *Hacker and Abers* [2004], seismic properties were calculated at 0.3 GPa and 120°C for basaltic and gabbroic compositions which are likely in the lower crust of the overriding plate. Theoretical *P* velocities of 7.06 km/s (basalts) to 7.16 km/s (gabbros) decrease to 6.94 km/s under prehnite-pumpellyite facies and to 6.45 km/s under zeolite facies, respectively, 2–3% to 8–10% lower. Our seismic model exhibits velocities lower than those inferred from *Hacker and Abers* [2004] for non-porous basalts and gabbros. According to measurements on oceanic basalt samples, a seismic velocity of 5.5 to 6.0 km/s is consistent with a porosity ranging from 3 to 6% [*Tsuji and Iturrino*, 2008].

During the subduction process, the subducting lithosphere, including the oceanic crust and possibly associated oceanic sediments, is subject to increasing temperature and pressure conditions. During this process,

free water, which exist in sediments and the highly porous upper oceanic crust, is first expelled by compaction and decrease of porosity related to the increase of lithostatic pressure. Deeper along the interplate boundary, where the temperature reaches 100 to 150°C, the dehydration of clays will provide additional free water [e.g., *Hyndman et al*., 1997]. The decrease of seismic velocity of ~5–6% observed in our low-velocity zone is consistent with the hydrothermal alteration of the mafic basement of the upper plate under zeolite or prehnite-pumpellyite facies conditions. Water released by the subducting plate and percolating upward leads to mineral alteration and hydration of the mafic and ultramafic rocks of the upper plate basement.

Similar supra-subduction LVZ is often described along active margins consisting of island arc or oceanic plateau sequence. Along the Cascadia margin, where the accreted fore-arc basement is mainly basaltic and gabbroic, the low *Vs* and high *Vp/Vs* ratios support a fluid-rich lower crust but do not preclude the hydration and alteration of mafic plutons and possible ultramafic cumulates [*Lees and Crosson*, 1990; *Tréhu et al*., 1994; *Parsons et al*., 1998; *Calkins et al*., 2011]. The ophiolitic Nicaragua and Costa Rica margin [*Christeson et al*., 1999; *Walther et al*., 2000; *Meléndez et al*., 2010] as well as the North Chile margin, offshore Antofagasta, which consists of arc-type basaltic igneous basement similar to the Jurassic magmatic arc of the La Negra formation which crops out along the coastal regions [*Sallarés and Ranero*, 2005], exhibit a 4 to 20 km thick layer above the interplate boundary, in which seismic velocities are several percent lower than the velocity in the layer immediately above. In both cases the alteration and hydration of the mafic to ultramafic crustal wedge by water released by subduction likely contribute to the observed low-velocity zone.

It has been proposed that overpressured fluids expelled along the subduction channel may hydrofracture the base of the overriding plate, thus promoting basal tectonic erosion [*Ranero et al*., 2008; *von Huene and Ranero*, 2003]. Nevertheless, fluids must reach a pressure higher than the lithostatic pressure to efficiently fracture rocks, and geophysical evidence indicates that hydrofracturing processes may penetrate only a few 100 m into the margin basement [e.g., *Sage et al*., 2006] whereas our LVZ is likely several kilometers thick even when the vertical smearing of the anomaly due to the limited resolution of our velocity model is taken into account.

The Carnegie Ridge was subducted beneath the study area in the past [*Michaud et al*., 2009; *Collot et al*., 2008]. Numerical modeling suggests that the subduction of oceanic plateaus and ridges will possibly lead to underplating of faulted blocks of the crust of the incoming plate mixed with sediments [e.g., *Tetreault and Buiter*, 2012]. Some seismic evidence for along-strike variation in the nature of material in the subduction channel at seismogenic depths has been described beneath Japan [*Kimura et al*., 2010] and Cascadia [*Tréhu et al*., 2012] suggesting that basement rocks from the subducting plate as well as sediments can be underplated beneath the leading edge of the fore-arc basement at depths of 10–20 km. There is also evidence for velocity inversions at greater depth beneath the fore arc (20–40 km) that have been attributed to underplated sediment [e.g., *Tréhu et al*., 1994; *Calvert et al*., 2011]. In the study area, most of the sediments of the incoming plate are subducted and possibly partly underplated at depth [*Collot et al*., 2008; *Agudelo et al*., 2009]. The velocities observed in the LVZ are consistent with terrigenous metasediments for which *Vp* averages 5.4–6.5 km/s [*Abers et al*., 2009]. At shallow depths ($<$10 km), pore waters are expelled by sediment compaction and bound water is released at T ~ 80–150°C (Figure 10) during the transformation of opal to quartz and clay to mica [*Peacock*, 2003]. Transient underplating of sediments beneath the inner wedge is described from deep seismic imaging and possibly control the broad 250 m high and recent seafloor swell observed in the bathymetry [*Collot et al*., 2008]. Nevertheless, the thickness of underplated sediments is less than 1 km thick [*Collot et al*., 2008] and cannot account for the up to 5 km thick LVZ described in our model.

Among the different hypotheses discussed in this chapter, we favor the hypothesis of the alteration and low grade metamorphism of the mafic and ultramafic rocks of the upper plate by fluids expelled from the incoming sediments and oceanic crust. It is likely the primary factor in the existence of the up to 5 km thick LVZ but we do not preclude additional processes like hydrofacturing and underplating.

6. Conclusions

Our 3-D tomographic velocity model highlights the 3-D structure of the Colombia-Ecuador subduction margin from 0°30′S to 2°30′N and encompasses the rupture zone of the 1958 earthquake, the southern part of the 1979 earthquake rupture zone to the north, and the transition to the 1942 rupture zone to the south (Figure 11).

The low vertical velocity gradient of the outer margin wedge, inferred from our tomographic model, coincides with the trenchward limit of the 1958 earthquake rupture zone. The low seismic velocities suggest that the outer margin wedge is weak, consisting likely of highly fractured rocks. Consequently, we suggest that the low rigidity of this outer wedge dissipated most of the seismic energy of the earthquake contributing to the coseismic deformation and uplift of the wedge. This explains the limited extension of the 1958 earthquake toward the trench and it is also possibly the cause of the tsunami associated with this event.

The low-velocity gradient outer wedge extends to the north updip of the first rupture phase of the 1979 earthquake [*Beck and Ruff*, 1984]. Assuming a similar process to the one described for the 1958 rupture and using the 1979 aftershocks (Figure 11), we suggest this first phase of the 1979 seismic rupture propagate into the outer margin wedge in a similar way to the 1958 rupture. The length of this first seismic rupture, well defined by seismograms [*Beck and Ruff*, 1984], coincides with the along-strike extension of the outer margin wedge inferred from our data set.

At depth, a 5 km thick low-velocity zone is observed immediately above the interplate contact. Because similar low-velocity zones are commonly observed along margins consisting of oceanic or island arc accreted terranes, we propose that this low-velocity zone results from the alteration and hydration of mafic and ultramafic rocks of the overlying basement rather than to hydrofracturing alone. Sediments underplated beneath the inner wedge [*Collot et al*., 2008] may contribute to this low-velocity zone but it is unlikely that they reach several kilometers thick. Nevertheless, fluids expelled by the compaction and dehydration of underplated sediments possibly favor the alteration of overlying rocks.

The low-velocity zone is also spatially coincident with the 1958 rupture zone. The connection with the 1958 rupture zone is uncertain, but might be related to the mechanical properties of rocks at the interplate boundary. For example, *Liu and Rice* [2009] show that friction data for gabbro gouge fit observations of slow deformation in northern Cascadia much better than do the granite data.

These results are in good agreement with the hypothesis that the rupture zone of great subduction earthquakes are partly controlled by upper plate structures [*Collot et al*., 2004]. The use of 3-D seismic data provides important constraints on the along-strike extension of several long wavelength features of the margin and allows better comparison with the rupture of the major interplate earthquakes.

Acknowledgments

This work is dedicated to our friend Bernard Pontoise, co-chief scientist onboard the R/V *Atalante* during the Esmeraldas cruise in 2005, who passed away in 2008. The Esmeraldas-2005 experiment was funded by the Institut de Recherche pour le Développement (IRD) and the Institut National des Sciences de l'Univers (INSU - CNRS). The experiment at sea was also supported by IFREMER, which provided the R/V *Atalante* for OBS deployment and shooting, and by DIMAR which provided R/V *Providencia* for OBS recovery. We also thanks INOCAR which provided us facilities to prepare the OBS in Guayaquil and to work in Ecuadorian waters. L.C. García Cano was supported by a grant of the "Département Soutien Formation" (DSF) of IRD. We are also indebted to the master and crew of the R/V *Atalante* as well as to the master and crew of the R/V *Providencia* for their support during the experiment, to Y. Hello, A. Anglade, and B. Yates who operated successfully the OBS at sea, to the scientific team onboard R/V *Atalante* and *Providencia* and to the scientific team which operated the seismometers on-land in difficult weather conditions. We also thank J.Y. Collot and N. Béthoux for their comments, V. Sallarés, A.J. Calvert, A. Tréhu, M. Nedimovic, and an anonymous reviewer for their careful review and English editing of the first version of this manuscript.

References

Abers, G. A., L. S. MacKenzie, S. Rondenay, Z. Zhang, A. G. Wech, and K. C. Creager (2009), Imaging the source region of Cascadia tremor and intermediate-depth earthquakes, *Geology*, *37*(12), 1119–1122, doi:10.1130/G30143A.1.

Agudelo, W., A. Ribodetti, J.-Y. Collot, and S. Operto (2009), Joint inversion of multichannel seismic reflection and wide-angle seismic data: Improved imaging and refined velocity model of the crustal structure of the north Ecuador–south Colombia convergent margin, *J. Geophys. Res.*, *114*, B02306, doi:10.1029/2008JB005690.

Barragan, B. E., G. M. Giaccio, and R. L. Zerbino (2001), Fracture and failure of thermally damaged concrete under tensile loading, *Mat. Struct.*, *34*(239), 312–319.

Beck, S. L., and D. H. Christensen (1991), Rupture process of the February 4, 1965, Rat Islands earthquake, *J. Geophys. Res.*, *96*(B2), 2205–2221.

Beck, S. L., and L. J. Ruff (1984), The rupture process of the Great 1979 Colombia Earthquake: Evidence for the asperity model, *J. Geophys. Res.*, *89*(B11), 9281–9291.

Byrne, D. E., D. M. Davis, and L. R. Sykes (1988), Loci and maximum size of thrust earthquakes and the mechanics of the shallow region of subduction zones, *Tectonics*, *7*(4), 833–857.

Calkins, J. A., G. A. Abers, G. Ekstroem, K. C. Creager, and S. Rondenay (2011), Shallow structure of the Cascadia subduction zone beneath western Washington from spectral ambient noise correlation, *J. Geophys. Res.*, *116*, B07302, doi:10.1029/2010JB007657.

Calvert, A. J., L. A. Preston, and A. M. Farahbod (2011), Sedimentary underplating at the Cascadia mantle-wedge corner revealed by seismic imaging, *Nat. Geosci.*, *4*(8), 545–548, doi:10.1038/ngeo1195.

Carlson, R. L. (2003), Bound water content of the lower oceanic crust estimated from modal analyses and seismic velocities of oceanic diabase and gabbro, *Geophys. Res. Lett.*, *30*(22), 2142, doi:10.1029/2003GL018213.

Carlson, R. L., and D. J. Miller (2003), Mantle wedge water contents estimated from seismic velocities in partially serpentinized peridotites, *Geophys. Res. Lett.*, *30*(5), 1250, doi:10.1029/2002GL016600.

Cediel, F., R. P. Shaw, and C. Caceres (2003), Tectonic assembly of the northern Andean Block, in *The Circum-Gulf of Mexico and the Caribbean: Hydrocarbon Habitats, Basin Formation, and Plate Tectonics: AAPG Memoir 79*, edited by C. Bartolini, R. T. Buffler, and J. Blickwede, pp. 815–848.

Christeson, G. L., K. D. McIntosh, T. H. Shipley, E. R. Flueh, and H. Goedde (1999), Structure of the Costa Rica convergent margin, offshore Nicoya Peninsula, *J. Geophys. Res.*, *104*(B11), 25,443–25,468.

Cloos, M. (1992), Thrust-type subduction-zone earthquakes and seamount asperities: A physical model for seismic rupture, *Geology*, *20*(7), 601–604.

Cloos, M., and R. L. Shreve (1996), Shear-zone thickness and the seismicity of Chilean- and Marianas-type subduction zones, *Geology*, *24*(2), 107–110.

Collot, J. Y., P. Charvis, M.-A. Gutscher, S. Operto, and the Sisteur scientific party (2002), Exploring the Ecuador-Colombia active margin and inter-plate seismogenic zone, *Eos Trans. AGU*, *83*(17), 185,189–190.

Collot, J. Y., B. Marcaillou, F. Sage, F. Michaud, W. Agudelo, P. Charvis, D. Graindorge, M. A. Gutscher, and G. Spence (2004), Are rupture zone limits of great subduction earthquakes controlled by upper plate structures? Evidences from multichannel seismic reflection data acquired across the northern Ecuador—southwest Colombia margin, *J. Geophys. Res.*, *109*, B11103, doi:10.1029/2004JB003060.

Collot, J. Y., W. Agudelo, A. Ribodetti, and B. Marcaillou (2008), Origin of a crustal splay fault and its relation to the seismogenic zone and underplating at the erosional north Ecuador–south Colombia oceanic margin, *J. Geophys. Res.*, *113*, B12102, doi:10.1029/2008JB005691.

Collot, J. Y., F. Michaud, A. Alvarado, B. Marcaillou, M. Sosson, G. Ratzov, S. Migeon, A. Calahorrano, and A. Pazmiño (2009), Visión general de la morfología submarina del margen convergente de Ecuador-Sur de Colombia: Implicaciones sobre la transferencia de masa y la edad de la subducción de la Cordillera de Carnegie, in *Geologia y geofisica marina y terestre del Ecuador desde la costa continental hasta las islas Gapapagos*, edited by J.-Y. Collot, V. Sallarés, and A. Pazmiño, pp. 47–74, Publicacion CNDM-INOCAR-IRD, PSE001-09, Guayaquil, Ecuador.

De Vries, T. (1988), The geology of late Cenozoic marine terraces (tablazos) in northwestern Peru, *J. South Am. Earth Sci.*, *1*, 121–136.

Dumont, J. F., E. Santana, F. Valdez, J. P. Tihay, P. Usselmann, D. Iturralde, and E. Navarette (2006), Fan beheading and drainage diversion as evidence of a 3200–2800 BP earthquake event in the Esmeraldas-Tumaco seismic zone: A case study for the effects of great subduction earthquakes, *Geomorphology*, *74*, 100–123.

Evain, M., A. Galve, P. Charvis, M. Laigle, H. Kopp, W. Weinzierl, A. Hirn, E. Flueh, J. Gallart, and the Lesser Antilles Thales scientific party (2013), Structure of the Lesser Antilles subduction forearc and backstop from 3D seismic refraction tomography, *Tectonophysics*, *603*, 55–67, doi:10.1016/j.tecto.2011.09.021.

Flueh, E. R., J. Bialas, and P. Charvis (2001), FS Sonne Fahrtbericht SO 159, SALIERI, Cruise Report Rep., 256 pp., GEOMAR cruise report, Kiel.

Gailler, A. (2005), Structure de la marge d'Équateur-Colombie par modélisation des données de sismique grand-angle marines: Influence sur le fonctionnement de la subduction et la sismicité, Thèse de Doctorat, 226 pp., Université Nice Sophia Antipolis.

Gailler, A., P. Charvis, and E. Flueh (2007), Segmentation of the Nazca and South American plates along the Ecuador subduction zone from wide angle seismic profiles, *Earth Planet. Sci. Lett.*, *260*(3-4), 444–464.

García Cano, L. C. (2009), Imagerie sismique 3D de la zone de subduction à la frontière Colombie-Équateur, Thèse de Doctorat, 214 pp., Université Nice Sophia Antipolis.

Gerdom, M., A. Tréhu, E. Flueh, and D. Klaeschen (2000), The continental margin off Oregon from seismic investigations, *Tectonophysics*, *329*(1-4), 79–97, doi:10.1016/S0040-1951(00)00190-6.

Gutscher, M. A., J. Malavieille, S. Lallemand, and J. Y. Collot (1999), Tectonic segmentation of the North Andean margin: Impact of the Carnegie Ridge collision, *Earth Planet. Sci. Lett.*, *168*(3-4), 255–270.

Hacker, B. R., and G. A. Abers (2004), Subduction Factory 3: An Excel worksheet and macro for calculating the densities, seismic wave speeds, and H_2O contents of minerals and rocks at pressure and temperature, *Geochem. Geophys. Geosyst.*, *5*, Q01005, doi:10.1029/2003GC000614.

Hacker, B. R., G. A. Abers, and S. M. Peacock (2003), Subduction factory - 1. Theoretical mineralogy, densities, seismic wave speeds, and H_2O contents, *J. Geophys. Res.*, *108*(B1), 2029, doi:10.1029/2001JB001127.

Hello, Y., B. A. Yates, A. Anglade, A. Gailler, and P. Charvis (2006), Hippocampe: A new versatile ocean bottom seismometer, paper presented at EGU General Assembly 2006, European Geosciences Union, Vienna, Austria, 02 – 07 April 2006.

Hyndman, R. D., M. Yamano, and D. A. Oleskevich (1997), The seismogenic zone of subduction thrust faults, *Island Arc*, *6*(3), 244–260.

Ioualalen, M., G. Ratzov, J. Y. Collot, and E. Sanclemente (2011), The tsunami signature on a submerged promontory: The case study of the Atacames Promontory, Ecuador, *Geophys. J. Int.*, *184*(2), 680–688.

Jaillard, E., M. Ordonez, S. Benitez, G. Berrones, M. Jimenez, G. Montenegro, and I. Zambrano (1995), Basin development in an accretionnary, oceanic-floored fore-arc setting: Southern coastal Ecuador during late Cretaceaous – late Eocene time, in *Petroleum Basins of South America*, edited by A. J. Tankard, R. Suarez, and H. J. Welsink, pp. 615–632, American Association of Petroleum Geologists, Yacimientos Petroíferos Fiscales Bolivianos and Academia Nacional de Ciencias de Bolivia, Tulsa, Okla.

Jaillard, E., S. Benitez, and G. H. Mascle (1997), Palaeogene deformations of the forearc zone of south Ecuador in relation to the geodynamic evolution, *Bull. Soc. Geol. Fr.*, *168*(4), 403–412.

Kamei, R., R. G. Pratt, and T. Tsuji (2012), Waveform tomography imaging of a megasplay fault system in the seismogenic Nankai subduction zone, *Earth Planet. Sci. Lett.*, *317-318*, 343–353, doi:10.1016/j.epsl.2011.10.042.

Kanamori, H., and E. E. Brodsky (2004), The physics of earthquakes, *Rep. Prog. Phys.*, *67*(8), 1429–1496.

Kanamori, H., and K. C. McNally (1982), Variable rupture mode of the subduction zone along the Ecuador - Colombia Coast, *Bull. Seismol. Soc. Am.*, *72*(4), 1241–1253.

Kelleher, J. A. (1972), Rupture zones of large South-American earthquakes and some predictions, *J. Geophys. Res.*, *77*(11), 2087–2103.

Kerr, A. C., G. F. Marriner, J. Tarney, A. Nivia, A. D. Saunders, M. F. Thirlwall, and C. W. Sinton (1997), Cretaceous basaltic terranes in western Colombia: Elemental, chronological and Sr-Nd isotopic constraints on petrogenesis, *J. Petrol.*, *38*(6), 677–702.

Kimura, T., K. Koketsu, H. Miyake, C. Wu, and T. Miyatake (2010), Dynamic source modeling of the 1978 and 2005 Miyagi-oki earthquakes: Interpretation of fracture energy, *J. Geophys. Res.*, *115*, B08302, doi:10.1029/2009JB006758.

Kopp, H., W. Weinzierl, M. Laigle, A. Becel, A. Hirn, and E. R. Flueh (2011), Deep structure of the central Lesser Antilles Island Arc: Relevance for the formation of continental crust, *Earth Planet. Sci. Lett.*, *304*, 121–134.

Krabbenhoft, A., J. Bialas, H. Kopp, N. Kukowski, and C. Hubscher (2004), Crustal structure of the Peruvian continental margin from wide-angle seismic studies, *Geophys. J. Int.*, *159*(2), 749–764.

Lapierre, H., et al. (2000), Multiple plume events in the genesis of the peri-Caribbean Cretaceous oceanic plateau province, *J. Geophys. Res.*, *105*(B4), 8403–8421.

Lay, T., and H. Kanamori (1981), An asperity model of great earthquake sequences, in *Earthquake Prediction: An International Review, Maurice Ewing Series, AGU*, edited by D. Simpson and P. Richards, pp. 579–592, AGU, Washington, D. C.

Lees, J. M., and R. S. Crosson (1990), Tomographic imaging of local earthquake delay times for three-dimensional velocity variation in Western Washington, *J. Geophys. Res.*, *95*(B4), 4763–4776.

Liu, Y., and J. R. Rice (2009), Slow slip predictions based on granite and gabbro friction data compared to GPS measurements in northern Cascadia, *J. Geophys. Res.*, *114*, B09407, doi:10.1029/2008JB006142.

Lonsdale, P. (2005), Creation of the Cocos and Nazca plates by fission of the Farallon plate, *Tectonophysics*, *404*(3-4), 237–264.

Ma, S. (2012), A self-consistent mechanism for slow dynamic deformation and large tsunami generation for earthquakes in the shallow subduction zone, *Geophys. Res. Lett.*, *39*, L11310, doi:10.1029/2012GL051854.

Mamberti, M., H. Lapierre, D. Bosch, E. Jaillard, R. Ethien, J. Hernandez, and M. Polve (2003), Accreted fragments of the Late Cretaceous Caribbean- Colombian Plateau in Ecuador, *Lithos*, *66*(3-4), 173–199.

Manchuel, K., M. Regnier, N. Bethoux, Y. Font, V. Sallarés, J. Diaz, and H. Yepes (2011), New insights on the interseismic active deformation along the North Ecuadorian-South Colombian (NESC) margin, *Tectonics*, *30*, TC4003, doi:10.1029/2010TC002757.

Marcaillou, B. (2003), Régimes tectoniques et thermiques de la marge Nord Equateur – Sud Colombie (0°-3.5°N) – Implications sur la sismogenèse, Thèse de Doctorat thesis, Université Pierre et Marie Curie (Paris VI), Paris.

Marcaillou, B., G. Spence, J. Y. Collot, and K. L. Wang (2006), Thermal regime from bottom simulating reflectors along the north Ecuador-south Colombia margin: Relation to margin segmentation and great subduction earthquakes, *J. Geophys. Res.*, *111*, B12407, doi:10.1029/2005JB004239.

Marcaillou, B., G. Spence, K. Wang, J.-Y. Collot, and A. Ribodetti (2008), Thermal segmentation along the N. Ecuador-S. Colombia margin (1-4 degrees N): Prominent influence of sedimentation rate in the trench, *Earth Planet. Sci. Lett.*, *272*(1-2), 296–308.

Meléndez, A., V. Sallarès, C. Ranero, K. McIntosh, I. Grevemeyer, and M. Prada (2010), Constraints on the seismogenesis of the Nicaragua 1992 slow tsunamigenic earthquake based on seismic travel-time tomography models, paper presented at EGU General Assembly 2010.

Mendoza, C., and J. W. Dewey (1984), Seismicity associated with the great Colombia-Ecuador earthquakes of 1942, 1958, and 1979 - Implications for barrier models of earthquake rupture, *Bull. Seismol. Soc. Am.*, *74*(2), 577–593.

Michaud, F., J.-Y. Collot, A. Alvarado, E. López, and Scientific and technical staff from the INOCAR (2006), República del Ecuador: Batrimetria y Relieve Continental, IOA - CVM - 02 - POST.

Michaud, F., C. Witt, and J. Y. Royer (2009), Influence of the subduction of the Carnegie volcanic ridge on Ecuadorian geology: Reality and fiction, *GSA Mem.*, *204*, 217–228, doi:10.1130/2009.1204(10.

Moberly, R., G. L. Shepherd, and W. T. Coulbourn (1982), Forearc and other basins, continental margin of northern and southern Peru and adjacent Ecuador and Chile, in *Trench-Forearc Geology: Sedimentation and Tectonics on Modern and Ancient Active Plate Margins*, edited by J. K. Leggett, pp. 245–258, *Geol. Soc. Spec. Publ.*, London, U.K.

Moore, G. F., N. L. Bangs, A. Taira, S. Kuramoto, E. Pangborn, and H. J. Tobin (2007), Three-dimensional splay fault geometry and implications for tsunami generation, *Science*, *318*(5853), 1128–1131.

Nakamura, Y., P. L. Donoho, P. H. Roper, and P. McPherson (1987), Large-offset seismic surveying ocean-bottom seismographs and air guns: Instrumentation and field technique, *Geophysics*, *52*(12), 1601–1611.

Nocquet, J. M., P. Mothes, and A. Alvarado (2009), Geodesia, geodinámica y ciclo sísmico en Ecuador, in *Geologia y geofisica marina y terestre del Ecuador desde la costa continental hasta las islas Gapapagos*, edited by J.-Y. Collot, V. Sallarés, and A. Pazmiño, pp. 83–94, Publicacion CNDM-INOCAR-IRD, PSE001-09, Guayaquil, Ecuador.

Papadimitriou, E. E. (1993), Long-term earthquake prediction along the western coast of South-America and Central-America based on a time predictable model, *Pure Appl. Geophys.*, *140*(2), 301–316.

Parsons, T., A. M. Tréhu, J. H. Luetgert, K. Miller, F. Kilbride, R. E. Wells, M. A. Fisher, E. Flueh, U. S. ten Brink, and N. I. Christensen (1998), A new view into the Cascadia subduction zone and volcanic arc: Implications for earthquake hazards along the Washington margin, *Geology*, *26*(3), 199–202.

Peacock, S. M. (2003), Thermal structure and metamorphic evolution of subducting slabs, in *Inside the Subduction Factory*, Geophys. Monogr. Ser., vol. 138, edited by J. Eiler, pp. 7–22, AGU, Washington, D. C., doi:10.1029/138GM02.

Pedoja, K., J. F. Dumont, M. Lamothe, L. Ortlieb, J. Y. Collot, B. Ghaleb, M. Auclair, V. Alvarez, and B. Labrousse (2006), Plio-Quaternary uplift of the Manta Peninsula and La Plata Island and the subduction of the Carnegie Ridge, central coast of Ecuador, *J. South Am. Earth Sci.*, *22*(1-2), 1–21.

Ranero, C. R., and R. von Huene (2000), Subduction erosion along the Middle America convergent margin, *Nature*, *404*(6779), 748–752.

Ranero, C. R., I. Grevemeyer, H. Sahling, U. Barckhausen, C. Hensen, K. Wallmann, W. Weinrebe, P. Vannucchi, R. von Huene, and K. McIntosh (2008), Hydrogeological system of erosional convergent margins and its influence on tectonics and interplate seismogenesis, *Geochem. Geophys. Geosyst.*, *9*, Q03S04, doi:10.1029/2007GC001679.

Ratzov, G., J. Y. Collot, M. Sosson, and S. Migeon (2010), Mass-transport deposits in the northern Ecuador subduction trench: Result of frontal erosion over multiple seismic cycles, *Earth Planet. Sci. Lett.*, *296*(1-2), 89–102.

Révillon, S., N. T. Arndt, C. Chauvel, and E. Hallot (2000), Geochemical study of ultramafic volcanic and plutonic rocks from Gorgona Island, Colombia: The plumbing system of an oceanic plateau, *J. Petrol.*, *41*(7), 1127–1153.

Reynaud, C., E. Jaillard, H. Lapierre, M. Mamberti, and G. H. Mascle (1999), Oceanic plateau and island arcs of southwestern Ecuador: Their place in the geodynamic evolution of northwestern South America, *Tectonophysics*, *307*(3-4), 235–254.

Ruff, L. J. (1989), Do trench sediments affect great earthquake occurrence in subduction zones, *Pure Appl. Geophys.*, *129*(1-2), 263–282.

Ryan, H. F., and D. W. Scholl (1993), Geologic implications of great interplate earthquakes along the Aleutian arc, *J. Geophys. Res.*, *98*(B12), 22,135–22,146.

Sage, F., J. Y. Collot, and C. R. Ranero (2006), Interplate patchiness and subduction-erosion mechanisms: Evidence from depth-migrated seismic images at the central Ecuador convergent margin, *Geology*, *34*(12), 997–1000.

Sallarés, V., and C. R. Ranero (2005), Structure and tectonics of the erosional convergent margin off Antofagasta, north Chile (23 degrees 30' S), *J. Geophys. Res.*, *110*, B06101, doi:10.1029/2004JB003418.

Sallarés, V., and P. Charvis (2003), Crustal thickness constraints on the geodynamic evolution of the Galapagos Volcanic Province, *Earth Planet. Sci. Lett.*, *214*(3-4), 545–559.

Schimmel, M., and J. Gallart (2007), Frequency-dependent phase coherence for noise suppression in seismic array data, *J. Geophys. Res.*, *112*, B04303, doi:10.1029/2006JB004680.

Tang, G. Y., et al. (2013), 3-D active source tomography around Simeulue Island offshore Sumatra: Thick crustal zone responsible for earthquake segment boundary, *Geophys. Res. Lett.*, *40*, 48–53, doi:10.1029/2012GL054148.

Tetreault, J. L., and S. J. H. Buiter (2012), Geodynamic models of terrane accretion: Testing the fate of island arcs, oceanic plateaus, and continental fragments in subduction zones, *J. Geophys. Res.*, *117*, B08403, doi:10.1029/2012JB009316.

Tréhu, A. M., I. Asudeh, T. M. Brocher, J. H. Luetgert, W. D. Mooney, J. L. Nabelek, and Y. Nakamura (1994), Crustal architecture of the Cascadia fore-arc, *Science*, *266*(5183), 237–243.

Tréhu, A. M., R. J. Blakely, and M. C. Williams (2012), Subducted seamounts and recent earthquakes beneath the central Cascadia forearc, *Geology*, *40*(2), 103–106, doi:10.1130/G32460.1.

Trenkamp, R., J. N. Kellogg, J. T. Freymueller, and H. P. Mora (2002), Wide plate margin deformation, southern Central America and northwestern South America, CASA GPS observations, *J. South Am. Earth Sci.*, *15*(2), 157–171.

Tsuji, T., and G. J. Iturrino (2008), Velocity-porosity relationships in oceanic basalt from eastern flank of the Juan de Fuca Ridge: The effect of crack closure on seismic velocity, *Explor. Geophys.*, *39*(1), 41–51.

Tsuji, Y., H. Matsutomi, F. Imamura, M. Takeo, Y. Kawata, M. Matsuyama, T. Takahashi, Sunarjo, and P. Harjadi (1995), Damage to coastal villages due to the 1992 Flores Island earthquake tsunami, *Pure Appl. Geophys.*, *144*(3-4), 481–524.

Vidale, J. E. (1990), Finite-difference calculation of traveltimes in three dimensions, *Geophysics*, *55*, 521–526.

von Huene, R., and C. R. Ranero (2003), Subduction erosion and basal friction along the sediment-starved convergent margin off Antofagasta, Chile, *J. Geophys. Res.*, *108*(B2), 2079, doi:10.1029/2001JB001569.

Walther, C. H. E., E. R. Flueh, C. R. Ranero, R. von Huene, and W. Strauch (2000), Crustal structure across the Pacific margin of Nicaragua: Evidence for ophiolitic basement and a shallow mantle sliver, *Geophys. J. Int.*, *141*(3), 759–777.

Wells, R. E., R. J. Blakely, Y. Sugiyama, D. W. Scholl, and P. A. Dinterman (2003), Basin-centered asperities in great subduction zone earthquakes: A link between slip, subsidence, and subduction erosion?, *J. Geophys. Res.*, *108*(B10), 2507, doi:10.1029/2002JB002072.

Westbrook, G. K., N. C. Hardy, and R. P. Heath (1995), Structure and tectonics of the Panama-Nazca plate boundary, in *Geologic and Tectonic Development of the Caribbean Plate Boundary in Southern Central America*, GSA Special Paper, edited by P. Mann, pp. 91–109.

White, S. M., R. Trenkamp, and J. N. Kellogg (2003), Recent crustal deformation and the earthquake cycle along the Ecuador-Colombia subduction zone, *Earth Planet. Sci. Lett.*, *216*(3), 231–242.

Zelt, C. A., and P. J. Barton (1998), Three-dimensional seismic refraction tomography: A comparison of two methods applied to data from the Faeroe Basin, *J. Geophys. Res.*, *103*(B4), 7187–7210.

Zelt, C. A., A. M. Hojka, E. R. Flueh, and K. D. McIntosh (1999), 3D simultaneous seismic refraction and reflection tomography of wide-angle data from the central Chilean margin, *Geophys. Res. Lett.*, *26*(16), 2577–2580.